Kovove Mater. 63 2025 195–206
DOI: 10.31577/km.2025.4.195

Effect of laser beam power ratio on microstructural evolution and mechanical properties in dual beam laser welding of duplex stainless steels

Lucia Kopčanová[1,2]*, Naďa Beronská[1], Miroslav Čavojský[1], Tomáš Dvorák[1], Erika Hodúlová[1]

[1] *Slovak Academy of Sciences, Institute of Materials and Machine Mechanics, Dúbravská cesta 9, 845 13 Bratislava, Slovak Republic*
[2] *Slovak University of Technology, Faculty of Mechanical Engineering, Námestie slobody 2910/17, 812 31 Bratislava, Slovak Republic*

Received 13 August 2025, received in revised form 7 October 2025, accepted 13 October 2025

Abstract

In this study, the influence of the dual-beam energy ratio on weld metal geometry, microstructural evolution, and mechanical performance was investigated for two duplex stainless steels: 2507 type super duplex, 2304 type lean duplex, and their combination. Butt joints in 5 mm thick sheets were produced using an IPG YLS-5000 fiber laser equipped with a twin-spot module, with a beam power ratio of 50 : 50 and 65 : 35. Weld cross-sections were analyzed using optical and scanning electron microscopy, phase fractions were quantified by image analysis, and mechanical properties were assessed via Vickers hardness mapping and room-temperature tensile tests. A 65 : 35 split concentrated energy in the primary beam, narrowing the bead by up to 33 % and deepening penetration by up to 329 %, while accelerating cooling to refine ferrite dendrites, suppress coarse boundary austenite, and shift phase balance toward higher ferrite contents (up to +10 %). These microstructural changes moderated weld metal hardness, bringing 2507 type super duplex steel closer to base-metal levels, and promoted mixed-mode fracture with smaller, more uniform dimples in a combination of 2507 type super duplex and 2304 type lean duplex steels, exhibiting the highest toughness under primary beam dominance. The results demonstrate that precise control of beam power ratio enables tailored duplex weld microstructures and properties, offering a route to optimize joint performance in demanding applications.

K e y w o r d s: dual beam laser welding, duplex stainless steel, austenite, ferrite

1. Introduction

Duplex stainless steels exhibit a dual-phase γ-austenite/δ-ferrite microstructure, typically near a 50 : 50 percent ratio, that combines high mechanical strength with excellent corrosion resistance. In welded joints, however, maintaining at least ~ 30 % austenite in the weld metal is essential, as lower γ fractions result in significant reductions in impact toughness and pitting resistance [1, 2]. This phase balance is critical in demanding environments such as offshore platforms and chemical processing plants, where localized corrosion can lead to failures [3, 4]. Moreover, the ferrite-austenite ratio influences thermal expansion behavior, affecting residual stress development during cooldown [5, 6].

Conventional single-beam laser welding, with its very high cooling rates, often yields fusion zones containing only 20–25 vol.% γ, since the rapid solidification suppresses the $\delta \rightarrow \gamma$ transformation [7, 8]. Such ferrite-rich welds are prone to nitride precipitation, brittle fracture, and localized corrosion attacks [9, 10]. Attempts to restore austenite through preheating or post-weld heat treatments can be partially effective,

*Corresponding author: tel.: +421 23240 1119; e-mail address: lucia.kopcanova@savba.sk

but they increase processing time and cost [11]. In addition, excessive heat input can cause grain coarsening in the heat-affected zone, which further reduces toughness [12].

Strategies to increase austenite content in single-beam processes, such as nitrogen-enriched shielding gas or in-situ laser reheating, can raise γ fractions to approximately 55 % in super duplex grades by enhancing nitrogen solubility and promoting diffusion-driven phase transformation [13, 14]. However, these methods typically require complex gas-handling systems or multi-pass heating cycles, which limit their industrial applicability. They may also increase the risk of porosity if the gas flow is not precisely controlled [15]. Furthermore, multi-pass approaches may yield heterogeneous microstructures, complicating subsequent machining and inspection.

Dual-beam laser welding could address critical challenges in duplex stainless steels, namely the difficulty of achieving high γ-austenite fractions without excessive heat input. To date, state-of-the-art reviews and experimental studies on duplex grades, such as 2507 type super duplex stainless steel (SDSS 2507) and 2304 type lean duplex stainless steel (LDSS 2304), make little or no mention of dual beam approaches, focusing instead on single-beam modifications such as shielding gas alloying or multi-pass reheating. Nevertheless, dual-beam processing offers several unique advantages for duplex alloys [16, 17]. First, by independently controlling the power density in the core and ring beams, it is possible to tailor the thermal profile to promote $\delta \rightarrow \gamma$ transformation kinetics during solidification, directly targeting the weld metal phase balance. Second, this split-mode heating can reduce thermal gradients and lower peak temperatures in the heat-affected zone, thereby minimizing grain coarsening and preserving toughness and corrosion resistance in the adjacent base material [18].

Beyond microstructural control, dual-beam welding also offers the potential to improve key mechanical and corrosion-related properties. More uniform γ/δ distributions can enhance impact toughness and pitting resistance, while stabilized keyholes can reduce spatter, porosity, and undercut defects that act as initiation sites for corrosion. Lower residual stresses and distortion make post-weld machining and inspection easier, further reducing production costs. In summary, dual-beam welding could deliver superior joint performance in duplex steels by combining deep penetration with precise phase-fraction tuning, offering advantages that are absent in current single-beam state-of-the-art methods [19, 20].

The dual-beam configuration is based on a coaxial arrangement, in which a high-power Gaussian core provides weld penetration, while an annular ring, typically operating at 20–40 % of the core's power, provides controlled reheating of the solidifying metal. This "adjustable-mode" design enables real-time modulation of the cooling rate by varying the ring's intensity or dwell angle, offering a level of process flexibility that is not achievable with single-beam systems. Compared to single-beam welding, dual-beam systems have been shown in aluminum and titanium alloys to reduce distortion and porosity levels by half and to increase favorable phase fractions by 25–30 % without sacrificing welding speed [21–23]. These advantages indicate that dual-beam laser welding is a promising candidate for next-generation duplex steel fabrication.

This study aims to determine whether precise adjustment of the dual-beam energy ratio can improve the microstructure and mechanical properties of duplex stainless-steel welds compared to conventional single-beam welding. Two types of duplex stainless steels are examined to assess how changes in the energy ratio influence weld geometry, phase balance, and microstructure refinement through cooling rate control, and how these effects translate into hardness, toughness, and overall joint quality. The goal is to demonstrate that an optimized dual-beam energy ratio can deliver significant improvements over traditional single-beam processes, particularly for demanding industrial applications.

2. Experimental setup and methodology

The experiment utilized 2507 type super duplex stainless steel (SDSS 2507) (EN 1.4410, UNS S32750) and 2304 type lean duplex stainless steel (LDSS 2304) (EN 1.4362, UNS S32304) and their combination (DSS Combi), supplied by Outokumpu. Both materials were commercially available as hot-rolled sheets with a thickness of 5 mm. SDSS 2507 is a high-performance alloy with exceptional corrosion resistance and strength, making it suitable for demanding applications in harsh environments, such as offshore oil and gas platforms and the marine industry. LDSS 2304 combines ferritic and austenitic phases with lower alloying content, offering excellent corrosion resistance and mechanical properties for applications in chemical processing and construction. The chemical composition and mechanical properties, as specified in the manufacturer's datasheets, are presented in Tables 1 and 2. The chemical composition was verified using a SpectroMAXx LMX06 optical emission spectrometer. According to the datasheets, the manufacturer guarantees the ferrite content in the base material as measured by a ferritescope. For SDSS 2507, the ferrite content in the base material is 53 % and austenite 47 %, while for LDSS 2304, the ferrite content is 51 % and austenite content 49 %.

Welded butt joints were fabricated from commercially available hot-rolled sheets, cut to dimensions of $100 \times 100 \times 5\,\mathrm{mm}^3$. The dual-beam laser welding

Table 1. Chemical composition of SDSS 2507 and LDSS 2304 (wt.%)

	C	Mn	Si	P	S	Cr	Mo	Ni	Cu	N
SDSS 2507	0.01	0.64	0.27	0.03	0.001	24.90	3.70	5.50	0.27	0.29
LDSS 2304	0.02	1.37	0.63	0.03	0.001	23.80	0.55	4.30	0.28	0.19

Table 2. Mechanical properties of SDSS 2507 and LDSS 2304

Mechanical property	UTS (MPa)	YS (MPa)	A5 (%)	HBW
SDSS 2507	901	707	33	273
LDSS 2304	792	615	34	250

Table 3. Laser welding parameters

Material	Laser power (kW)	Welding speed ($mm\,s^{-1}$)	Shielding gas flow ($l\,min^{-1}$)	Defocusing distance (mm)	Beam power distribution ratio	Heat input ($kJ\,mm^{-1}$)
SDSS 2507	3400	10	0.3	0	50 : 50	0.34
LDSS 2304	3400	10	0.3	0	50 : 50	0.34
DSS COMBI	3400	10	0.3	0	50 : 50	0.34
SDSS 2507	3400	10	0.3	0	65 : 35	0.34
LDSS 2304	3400	10	0.3	0	65 : 35	0.34
DSS COMBI	3400	10	0.3	0	65 : 35	0.34

(DBLW) process was performed using an IPG YLS 5000 solid-state fiber laser at The First Welding Company, Inc. in Bratislava, operating at a wavelength of 1.06 μm with a maximum power output of 5 kW. The laser system was equipped with a Precitec YW52 welding head featuring a 200 mm collimation lens and a 150 mm focusing lens. A specialized twin-spot module integrated into the welding head splits the laser beam into two spots with a 1.7 mm separation in a tandem configuration. Welding parameters, including laser power, welding speed, shielding gas flow rate, and beam focus position, were kept constant for all three samples, while the energy distribution between the two beams was varied at ratios of 50 : 50 and 65 : 35. Nitrogen 5.0 was used as the shielding gas. The specific welding parameters are summarized in Table 3.

Transverse cross-sections were cut from the center of the butt joints to characterize weld formation, examine both macro- and microstructures, and evaluate microhardness. After sectioning, all specimens were mounted in conductive mounting material. Grinding and polishing were performed using an automatic grinder (Mecatech 334 SPC). Grinding was carried out with water-abrasive papers of progressively finer grit sizes (240, 400, 600, 800, and 1200), followed by polishing with diamond suspensions of 9, 6, 3, and 1 μm particle sizes applied in combination with appropriate polishing plates. The samples were then etched in Beraha's solution (30 ml HCl, 60 ml H_2O, and 1 g $K_2S_2O_5$) for approximately 5 seconds. Macroscopic analysis of the welds was conducted using a Carl Zeiss Axio Observer Z1m light microscope, while the microstructure was examined with a JEOL 7600F scanning electron microscope (SEM).

Tensile tests were performed at room temperature (≈ 23 °C) on a Zwick Roell 1474 testing machine in accordance with ASTM E8. For each set of welding parameters, three specimens were tested to evaluate the reproducibility of the dual-beam laser process. Percentage deviations beside each mean value indicate the spread of results, with all measured properties falling within a narrow tolerance of ± 2 %, confirming excellent repeatability of the welding conditions.

Vickers hardness was measured on metallographically prepared transverse sections using the 0.2 N load in accordance with STN EN ISO 6507-1, performed with an FM 100 tester equipped with a Future FM--ARS 9000a source.

3. Results and discussion

3.1. Cross-section of weld joints

The cross-sections in Fig. 1 show that increasing the energy split ratio from 50 : 50 to 65 : 35 shifts the weld from a wider surface bead to deeper penetration with a wider root. This effect is more pronounced in LDSS 2304 than in SDSS 2507 because LDSS 2304 has a thermal conductivity of approximately $17\,W\,m^{-1}\,K^{-1}$, about 13 % higher than the $15\,W\,m^{-1}\,K^{-1}$ measured for SDSS 2507. The higher

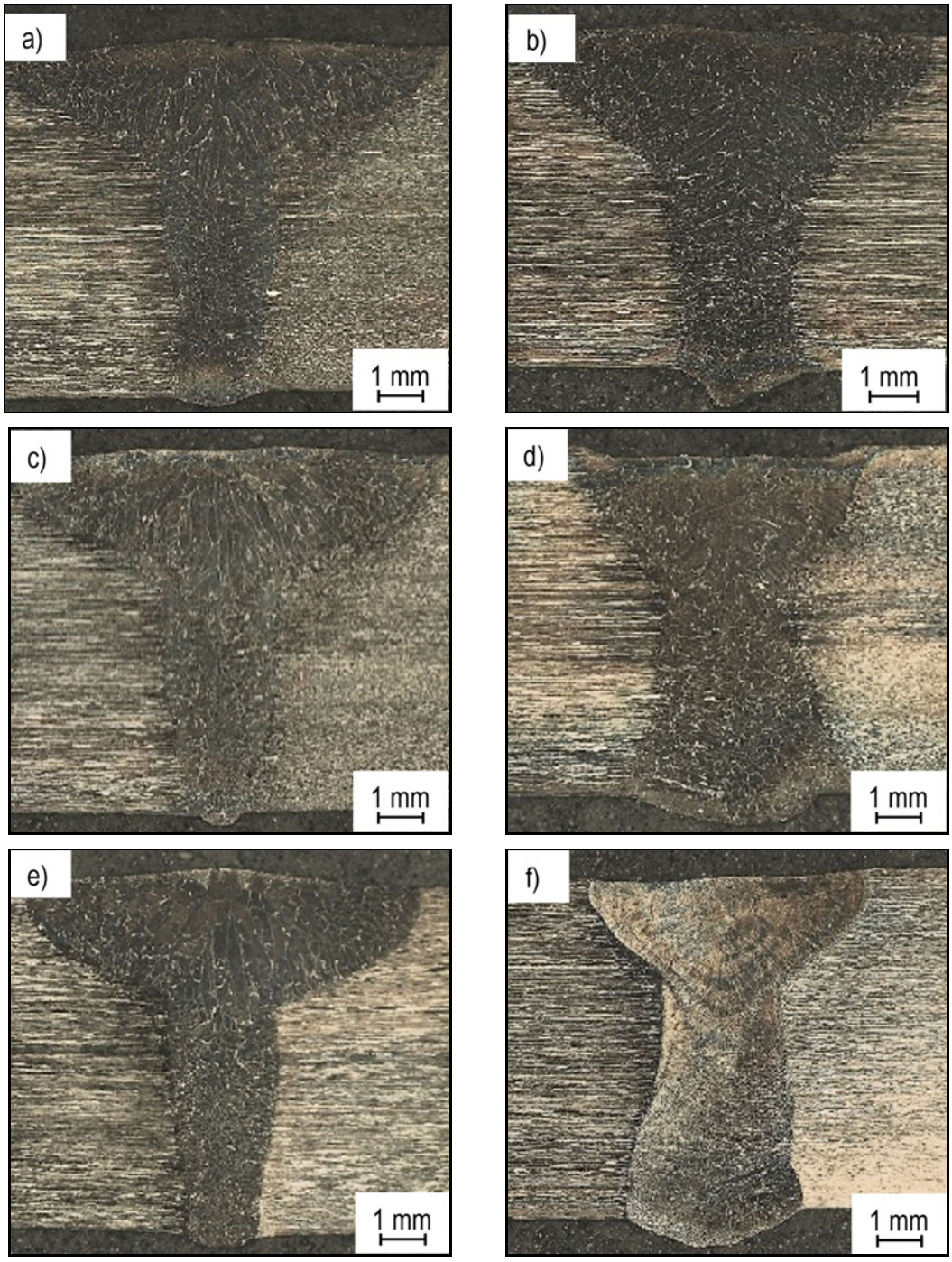

Fig. 1. Cross-sectional micrographs of butt-welded joints produced by dual-beam laser welding: (a) SDSS 2507 (50 : 50 beam power ratio), (b) SDSS 2507 (65 : 35 beam power ratio), (c) LDSS 2304 (50 : 50 beam power ratio), (d) LDSS 2304 (65 : 35 beam power ratio), (e) DSS COMBI (50 : 50 beam power ratio), and (f) DSS COMBI (65 : 35 beam power ratio).

thermal conductivity enables LDSS 2304 to dissipate heat more rapidly. At higher beam powers, this produces a steeper temperature gradient in the upper region of the weld pool, promoting melt convection toward the root and resulting in a more pronounced narrowing of the bead. Sun and Dilger [24] reported that changes in the temperature-dependent thermal conductivity of austenite are low and have a negligible influence on the expected weld size or cooling rate. In contrast, the significantly larger variations in the thermal conductivity of ferritic α-Fe have a substantial impact on the temperature field. By fine-tuning the beam energy ratio, the surface and root geometry of the weld can be precisely controlled, enabling optimization of the weld profile and mechanical properties in duplex stainless steels.

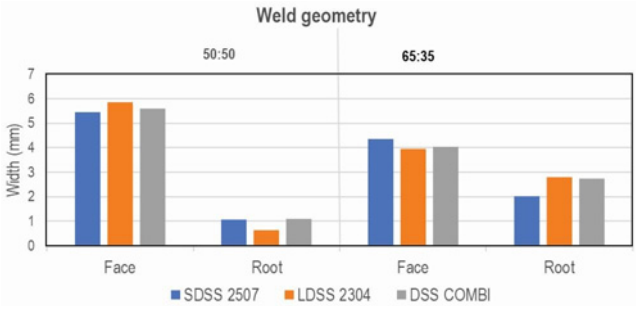

Fig. 2. Weld geometry: Measured bead widths at face and root side for SDSS 2507, LDSS 2304, and DSS COMBI under 50:50 and 65:35 beam power distribution ratios.

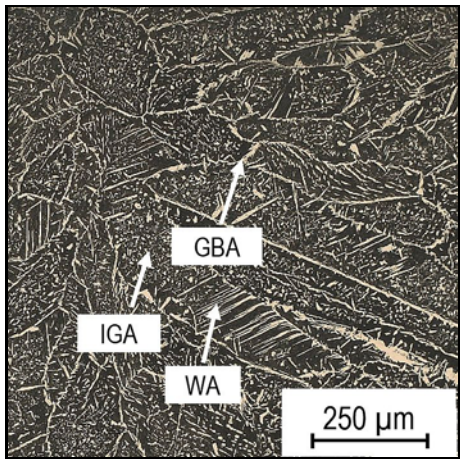

Fig. 3. Microstructure of weld metal: ferritic and austenitic grains.

Weld bead geometry was quantitatively assessed by measuring the surface bead width at the weld crown and the root bead width at the point of maximum penetration on cross-sections for two beam power distributions (50 : 50 and 65 : 35), as shown in Fig. 2. Changing the beam power ratio from 50 : 50 to 65 : 35 produced distinct effects in all three materials. In SDSS 2507, the surface bead width decreased from 5.44 to 4.36 mm (–19.9 %), while the root bead width increased from 1.08 to 2.03 mm (+88 %). LDSS 2304 showed the strongest response, with the bead width reduced from 5.86 mm to 3.96 mm (–32.4 %) and the root bead width increasing from 0.65 to 2.79 mm (+329 %). The DSS COMBI exhibited intermediate behavior, with the bead width narrowing from 5.59 to 4.04 mm (–27.7 %) and the root bead width expanding from 1.10 to 2.75 mm (+150 %). These results confirm that increasing the primary beam fraction leads to consistent narrowing of the weld and widening of the weld root, with the magnitude of these effects determined by the intrinsic thermal conductivity, solidification rate, and absorption characteristics of each alloy.

At a 50 : 50 split, the balanced power promotes a strong Marangoni flow [25, 26], producing a wide, shallow surface bead and limited root penetration. Switching to a 65 : 35 split deepens the keyhole, increasing downward metal flow (widening the root) but also raising back pressure and surface unevenness. LDSS 2304 shows the most pronounced bead-shape changes, due to its lower thermal conductivity, narrow solidification range, and associated keyhole deepening and instability. In contrast, SDSS 2507, with its higher thermal conductivity, dampens these extremes, while the combination of these materials exhibits intermediate behavior. Adapting the beam energy ratio to the specific thermal and metallurgical properties of each alloy is therefore essential for precise control of weld morphology.

In addition to differences in thermal conductivity and solidification range, several other physical mechanisms reported in the literature [27–29] help explain the observed changes in bead shape with varying beam energy ratios. A higher primary beam fraction deepens the keyhole, altering the inclination of its side walls and increasing the number of internal laser reflections. This enhances energy absorption in the lower region of the molten pool, driving metal flow toward the root. At the same time, the temperature gradient between the pool center and its periphery affects the temperature coefficient of surface tension. Depending on the sign of $d\gamma/dT$, Marangoni convection can be directed outward or inward, influencing both weld width and depth. Concentrating more energy in a narrower region also shifts heat transfer from being primarily conduction-controlled at lower primary beam fractions (50 : 50) to convection-dominated at higher fractions (65 : 35). This transition promotes deeper penetration and a narrower surface bead, as observed particularly in LDSS 2304.

3.2. Microstructural analysis of weld joints

Figure 3 shows the characteristic duplex microstructure of the weld metal, consisting of ferritic grains (dark contrast) and austenite (light contrast) formed under dual-beam laser welding conditions. Three austenite morphologies can be identified. Grain boundary austenite (GBA) forms coarse islands (10–20 µm) along ferrite grain boundaries, indicating heterogeneous nucleation in solute-enriched regions during slower local cooling. Intergranular austenite (IGA) appears as thin films (1–5 µm) along ferrite dendrite arms, consistent with formation in narrow, undercooled interdendritic channels. Widmanstätten austenite (WA) develops as plate-like intrusions (2–10 µm wide) extending inward from ferrite boundaries along preferred crystallographic planes, representing

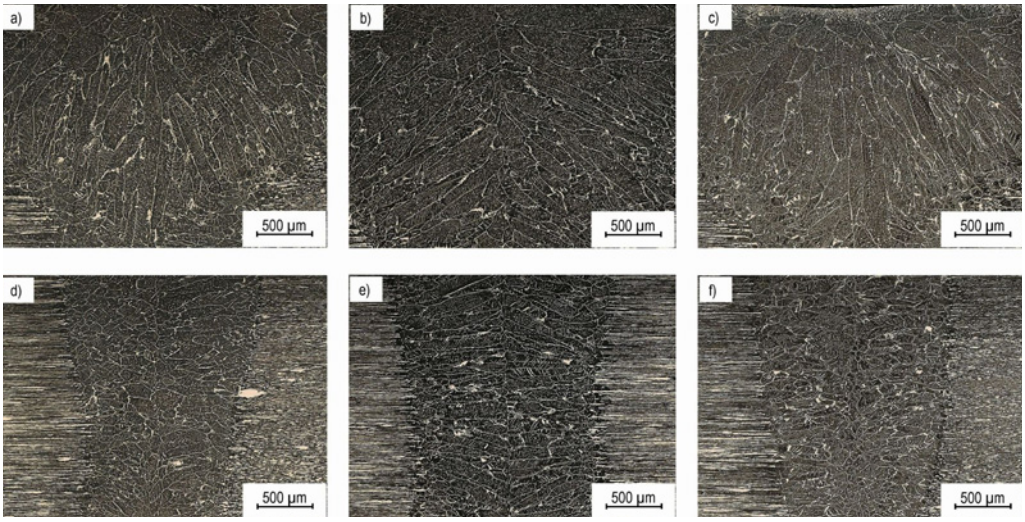

Fig. 4. Microstructural evolution across the weld bead: Face and root side under a 50:50 beam power ratio for (a) SDSS 2507 face side, (b) LDSS 2304 face side, (c) DSS COMBI face side, (d) SDSS 2507 root side, (e) LDSS 2304 root side, and (f) DSS COMBI root side.

a diffusion-controlled $\delta \rightarrow \gamma$ transformation during post-solidification cooling.

At a 50 : 50 beam energy ratio, slower cooling results in a higher fraction of GBA and coarser WA plates, reflecting longer transformation times. In contrast, the 65 : 35 configuration produces steeper thermal gradients and faster cooling rates, suppressing GBA coarsening and favoring finer WA and IGA morphologies. These changes are directly linked to the control of local solidification kinetics through precise adjustment of the beam energy ratio.

Figure 4 shows the microstructures of welded joints produced with a 50 : 50 beam power ratio for SDSS 2507, LDSS 2304, and the DSS COMBI. For clarity, the weld cross-sections are divided into upper and lower regions. In the upper area, the equiaxed duplex grains of the base material transition through a narrow HAZ (up to $\sim 100\,\mu m$), typical for laser welding, into thickened ferritic grains with austenite forming along grain boundaries and within ferritic grains. Grain width varies with alloy composition: SDSS 2507 exhibits the smallest widths, LDSS 2304 shows thicker grains, and DSS COMBI displays the most pronounced thickening (Figs. 4a–c).

In the lower region, ferritic grains change orientation and undergo significant refinement (Figs. 4d–f). Coarser grains are observed in SDSS 2507, finer in LDSS 2304, and the finest in DSS COMBI. This gradient in grain size reflects differences in thermal conductivity, solidification rate, and solute redistribution between the alloys. Such refinement in the lower weld zone is consistent with literature reports [30–32] showing that higher thermal gradients and faster solidification rates near the keyhole base promote finer ferritic grains and suppress excessive austenite coarsening.

Under the 65 : 35 laser energy distribution, the overall trends in grain morphology between alloys remain the same, but with notable differences from the 50 : 50 case. In the upper region, the ferritic grains are elongated in the direction of heat flow, but grain thickening is less pronounced, and solidification features are more directional (Figs. 5a–c). In the lower region, columnar grains extend toward the root, but without the significant refinement seen in the lower zone of the 50 : 50 condition (Figs. 5d–f).

The differences in grain morphology between the two energy ratios arise from variations in melt dynamics and cooling rates. At 50 : 50, the balanced energy distribution promotes strong Marangoni flow, increasing the molten pool's surface area and slowing solidification, which allows austenite and other phases to grow into larger, more equiaxed grains [33, 34]. At 65 : 35, a higher proportion of energy in the primary beam concentrates heat deeper in the molten pool, accelerating vertical heat removal, shortening cooling time, and reducing lateral pool spread. This faster solidification restricts grain growth and limits austenite formation, as the rapid cooling hinders the diffusion of alloying elements required for its stabilization [35, 36].

At a 50 : 50 beam power ratio, phase analysis of the fusion zone revealed ferrite contents of 64 % in SDSS 2507, 67 % in LDSS 2304, and 62 % in DSS COMBI, with corresponding austenite fractions of 36, 33, and 38 %, respectively. Increasing the ratio to 65 : 35 promoted ferrite stabilization. As shown in Fig. 6, the ferrite contents rose to 74 % in SDSS 2507, 66 % in LDSS 2304, and 64 % in DSS COMBI, while austenite fractions decreased to 26, 34, and 36 %. This trend confirms that concentrating energy in the primary beam elevates cooling rates and thermal gradients, favoring

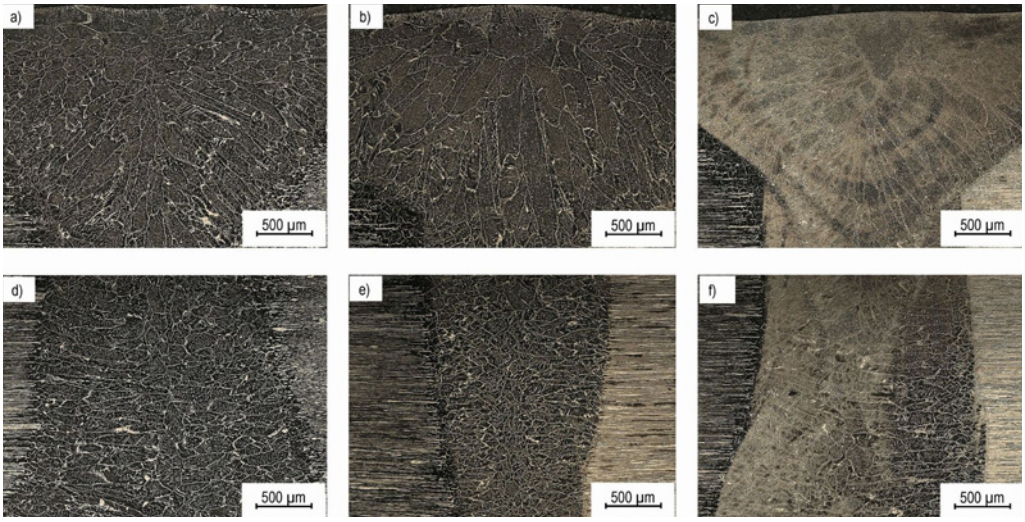

Fig. 5. Microstructural evolution across the weld bead: Face and root side under a 65 : 35 beam power ratio for (a) SDSS 2507 face side, (b) LDSS 2304 face side, (c) DSS COMBI face side, (d) SDSS 2507 root side, (e) LDSS 2304 root side, and (f) DSS COMBI root side.

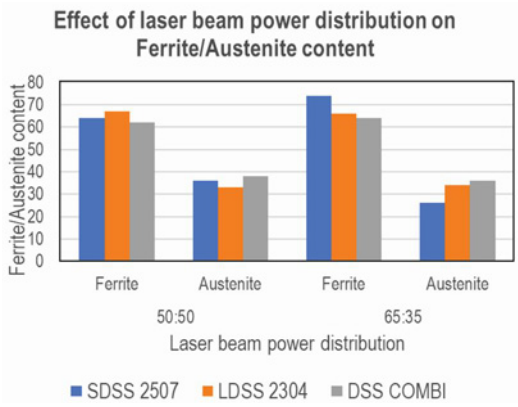

Fig. 6. Effect of dual beam power distribution (50 : 50 vs. 65 : 35) on ferrite and austenite phase fractions in SDSS 2507, LDSS 2304, and DSS COMBI welds.

rapid ferrite solidification and suppressing austenite formation in the weld metal. Therefore, optimization of dual-beam parameters must balance the desired phase composition with energy distribution to achieve the targeted combination of mechanical performance and corrosion resistance.

3.3. Mechanical properties

3.3.1. Tensile properties

Tensile tests were performed on dual-beam laser-welded specimens to evaluate their mechanical performance under different beam energy ratios. According to the Outokumpu datasheets, the base materials LDSS 2304 and SDSS 2507 exhibit tensile strengths of 792 MPa and 901 MPa, respectively, and elongations

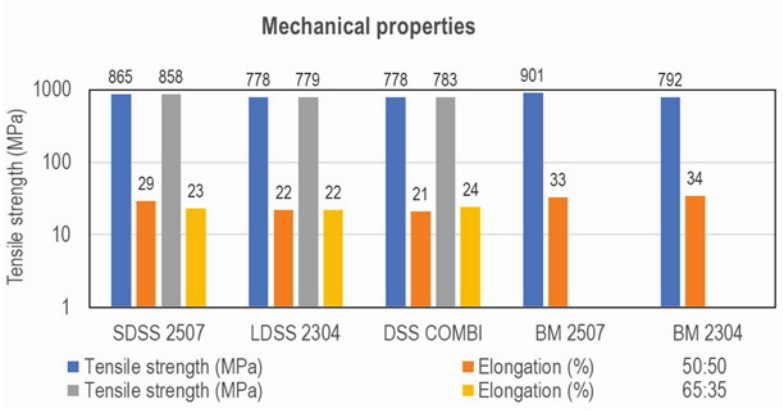

Fig. 7. Tensile test results of SDSS 2507, LDSS 2304, and DSS COMBI joints for various sample types: average tensile strength and elongation for beam power ratios of 50 : 50 and 65 : 35, including the base material values provided by the manufacturer.

of 34 % and 33 %, respectively.

In all cases, the stress–strain behavior showed a predominantly linear elastic region, followed by rapid failure, indicating limited energy absorption before failure. In comparison (Fig. 7), the SDSS 2507 sample showed the highest elongation among all tested joints, reaching 29 % and 23 %, respectively, and demonstrated a more gradual transition into the plastic region. All other samples (LDSS 2304 and DSS COMBI) showed the same strengths of 780 MPa and elongation of 22 %. All combined samples failed at the base of the LDSS 2304 material, demonstrating that its lower elongation and toughness make it the weakest link, while the weld metal and SDSS 2507 resist higher stress and deformation. Concentrating the beam from a 50 : 50 to a 65 : 35 split produces only marginal tensile-property changes because the overall fusion-zone thermal cycles remain similar, yielding comparable microstructures across splits. SDSS 2507 very slight drop in UTS (865 → 858 MPa) and elongation (29 → 23 %) reflects just enough grain-refinement and faster cooling under the deeper keyhole to reduce its strain-hardening capacity. By contrast, the DSS COMBI mixed alloy exhibits higher tensile strength (778 → 783 MPa) and improved elongation (21 → 24 %), consistent with the altered solidification in the hybrid zone that promotes a more favorable phase equilibrium. LDSS 2304, with its poor chemical composition and coarse grains, shows virtually no change in mechanical properties (778 → 779 MPa, 22 % elongation), because its melt dynamics and cooling behavior are inherently less sensitive to a 15 % energy shift.

Scanning electron micrographs of the tensile fracture surfaces reveal pronounced differences in failure mode and dimple morphology as a function of alloy composition and beam energy ratio. In all SDSS 2507 and LDSS 2304 joints, fractures occurred in the HAZ. For the DSS COMBI joints, fracture consistently initiated in the LDSS 2304 region, confirming that its lower ductility and toughness make it the limiting factor in the hybrid configuration.

Beam power ratio 50 : 50 at SDSS 2507 (Fig. 8a) exhibits deep, equiaxed microvoid dimples (1–3 μm) characteristic of ductile fracture in its coarse-grained fusion zone. LDSS 2304 (Fig. 8b) shows smaller, more uniformly distributed dimples (0.5–1.5 μm) with occasional shallow cleavage facets, reflecting its higher ferrite content and constrained void growth. The DSS COMBI (Fig. 8c) exhibits intermediate fractography, characterized by moderate-sized dimples (1–2 μm) and fine microvoid clusters, indicating a balanced toughness.

When the beam energy ratio is 65 : 35, the SDSS 2507 (Fig. 8d) transitions toward a mixed ductile-brittle fracture mode, featuring smaller, irregular dimples interspersed with quasi-cleavage facets, in agreement with its reduced elongation [37]. LDSS 2304 (Fig. 8e) at a beam energy ratio of 65 : 35 retains a predominantly ductile appearance but with marginally coarser dimples than in the 50 : 50 condition, consistent with the finer grain structure facilitating deeper void coalescence.

In contrast, DSS COMBI (Fig. 8f) displays the finest and most homogeneous dimple morphology at 65 : 35, with dense clusters of 0.5–1 μm voids and minimal cleavage, indicative of its superior toughness under primary-beam dominance.

These observations correlate directly with the underlying microstructural refinements induced by increased primary beam energy, which steepen thermal gradients and accelerate solidification. The varying dimple sizes and the presence or absence of cleavage facets across alloys and beam ratios underscore the critical role of phase balance, grain size, and residual stress in dictating fracture behavior. Consequently, optimizing dual-beam parameters enables the tailoring of both microstructure and mechanical performance in duplex stainless-steel welds.

Fracture morphology varies with microstructural refinement, phase balance, and residual stresses, as influenced by the beam energy ratio. At a 50 : 50 beam energy ratio, balanced heating yields coarser ferrite and grain-boundary austenite: in standard DSS, this produces deep, equiaxed dimples, while lean LDSS 2304, with more ferrite, limits void growth, giving smaller, uniform dimples with some cleavage facets. DSS COMBI intermediate chemistry delivers mixed dimples and microvoid clusters. Raising the primary beam to 65 : 35 intensifies cooling, refining ferrite, and reducing coarse austenite. SDSS 2507 then shows quasi-cleavage facets amid smaller dimples due to higher ferrite and tensile stresses; LDSS 2304 still forms deeper voids despite its ferrite-rich structure; DSS COMBI achieves the most uniform dimple pattern thanks to optimal grain refinement and phase distribution.

3.3.2. Vickers hardness

The microhardness curves for individual weld joints are shown in Fig. 9. In SDSS 2507, a 50 : 50 beam power ratio yields weld metal microhardness peaks of 270–280 HV, exceeding the BM microhardness of ∼ 260 HV and indicative of grain-boundary strengthening within the fusion zone. Adopting a 65 : 35 beam power ratio homogenizes the Vickers hardness profile of weld metal values, stabilizing at 255 to 265 HV, closely matching the base material, reflecting ferrite-grain refinement and reduced residual stresses under steeper thermal gradients.

LDSS 2304 remains largely unchanged due to its stable ferritic matrix. Both power distributions produce comparable hardness levels from 255 to 270 HV across the base material, HAZ, and weld metal. How-

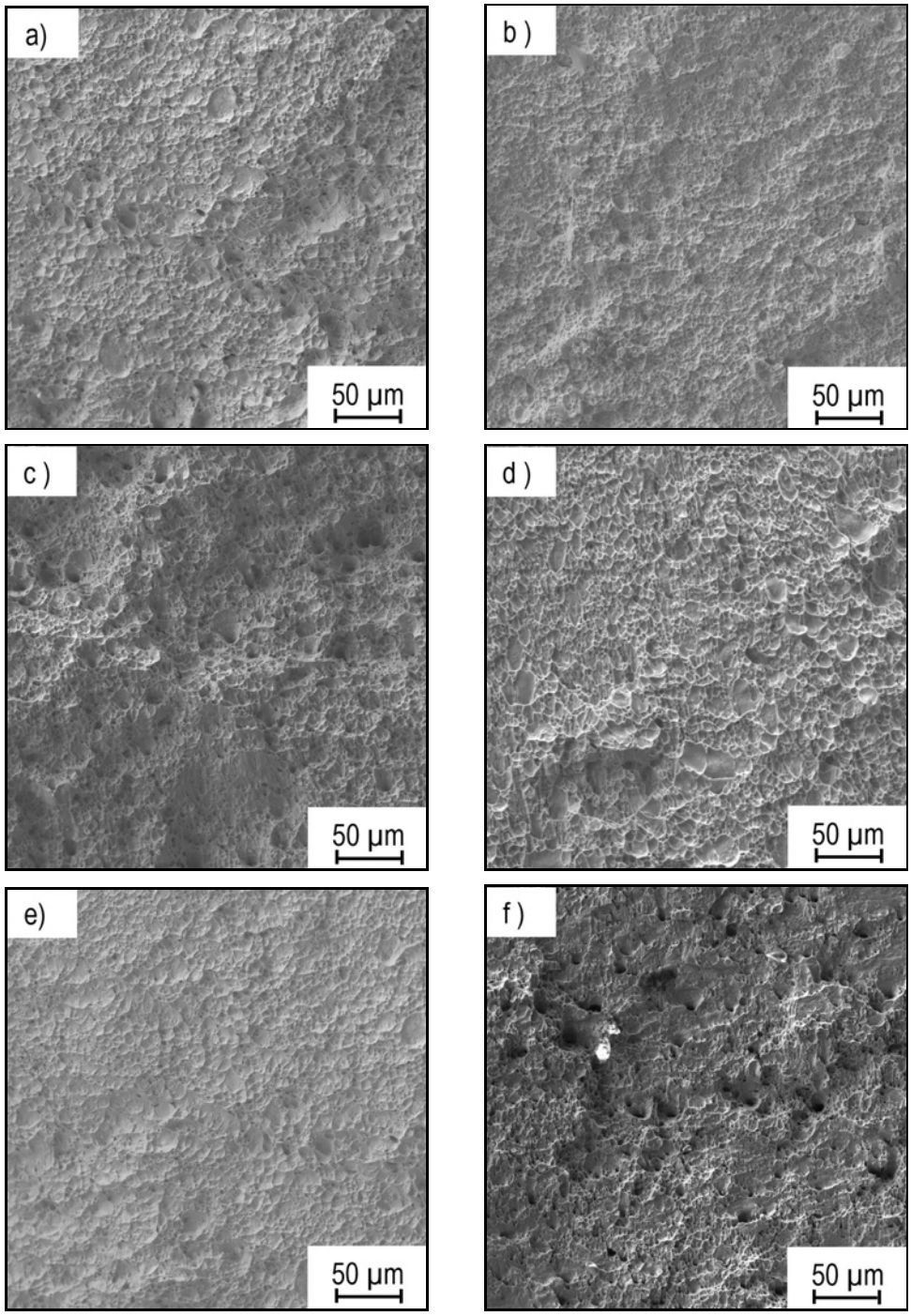

Fig. 8. Fractography: (a) SDSS 2507 (50 : 50 beam power ratio), (b) LDSS 2304 (50 : 50 beam power ratio), (c) DSS COMBI (50 : 50 beam power ratio), (d) SDSS 2507 (65 : 35 beam power ratio), (e) LDSS 2304 (65 : 35 beam power ratio), and (f) DSS COMBI (65 : 35 beam power ratio).

ever, the 65 : 35 condition exhibits slightly increased scatter in the weld region, consistent with its more heterogeneous intergranular austenite morphology.

For DSS COMBI, the 50 : 50 beam energy ratio generates the highest weld metal hardness peaks ($\sim$ 290–300 HV), attributable to grain boundary austenite and slower cooling rates, whereas the 65 : 35 beam power ratio lowers and smooths the profile from 270 to 285 HV, in agreement with its finer intergranular austenite and suppressed Widmanstätten austenite formation (Fig. 9).

Collectively, increasing the primary-beam fraction to 65 : 35 moderates weld metal hardening in all alloys by refining dendritic microstructures, optimizing phase balance, and mitigating residual stress accumulation. Hardness differences between 50 : 50 and 65 : 35

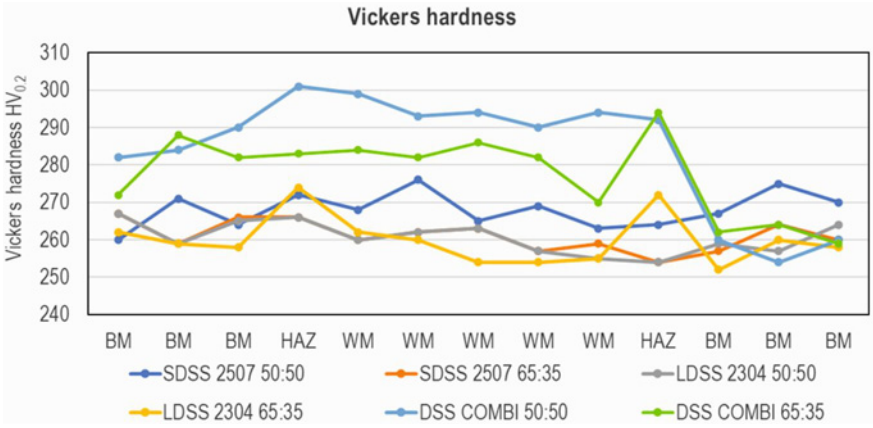

Fig. 9. Vickers hardness profiles across base metal (BM), heat-affected zone (HAZ), and weld metal (WM) for SDSS 2507, LDSS 2304, and DSS COMBI under 50 : 50 and 65 : 35 laser beam power ratios.

beam power ratios arise from their distinct thermal cycles and microstructures. A 50 : 50 beam power ratio balanced heating cools slowly, forming coarse columnar ferrite and grain boundary austenite that raise hardness via boundary strengthening and dislocation build-up. The 65 : 35 beam power ratio steeper thermal gradients speed solidification, refine ferrite grains and spacing, reduce tensile stresses, and limit dislocations, bringing weld hardness closer to the base metal [38, 39]. LDSS 2304's ferritic matrix shows little hardness change with beam energy ratio, while DSS COMBI drops in hardness under 65 : 35 as austenite refines into thin films. Therefore, optimization of the dual-beam energy ratio must balance hardness, toughness, and phase stability to meet the specific service requirements of duplex stainless-steel joints.

4. Conclusions

This study systematically investigated the influence of dual-beam power ratios (50 : 50 and 65 : 35) on weld geometry, microstructural evolution, and mechanical performance in duplex stainless steels: SDSS 2507, LDSS 2304, and their combination. The main findings of this study can be summarized as follows:

– Increasing the beam power ratio from 50 : 50 to 65 : 35 significantly modifies the weld bead profile, producing deeper penetration and a wider root, with the most pronounced effects observed in alloys with lower thermal conductivity, such as LDSS 2304.

– Changes in beam power distribution affect the microstructure. The 50 : 50 ratio, with slower cooling and balanced melt flow, promotes larger, more uniform grains and coarser grain-boundary and Widmanstätten austenite. The 65 : 35 ratio drives heat deeper, increases thermal gradients, speeds cooling, refines ferrite grains, promotes intragranular austenite films, limits austenite coarsening, and creates a more directional solidification pattern.

– Microscopic analysis shows that a 50 : 50 beam power ratio, with its slower cooling rates, allows larger austenite fractions to develop, whereas a 65 : 35 ratio accelerates cooling, enhances ferrite stability, and reduces austenite formation.

– The 50 : 50 and 65 : 35 beam power ratios produced similar tensile properties, with only minor changes between them. SDSS 2507 had the highest elongation and strength, DSS COMBI improved slightly at 65 : 35 due to a more favourable phase balance, and LDSS 2304 remained largely unchanged, confirming it as the weakest material. For both beam power distribution ratios, all alloys exhibited ductile fracture, with DSS COMBI showing the highest toughness, followed by SDSS 2507 and LDSS 2304.

– A 50 : 50 beam power split produces higher weld metal hardness, while a 65 : 35 split with a finer microstructure brings the weld metal hardness closer to that of the base metal. Among the alloys, SDSS 2507 and DSS COMBI show greater hardness variation between ratios, whereas LDSS 2304 remains largely unchanged due to its stable ferritic matrix.

– In summary, the dual-beam power ratio is a key parameter for optimizing weld metal characteristics in duplex stainless steels. Careful selection of the ratio allows control over bead geometry, microstructural refinement, phase balance, and mechanical properties while maintaining the base material composition and avoiding additional post-weld treatments.

Future work should explore real-time modulation of the beam power ratio and assess its influence on corrosion resistance, residual stress distribution, and fatigue performance.

Acknowledgements

This work was financially supported by the following funding bodies: the Slovak Research and Development Agency (APVV-21-0232), the Scientific Grant Agency of

the Ministry of Education, Science, Research, and Sport of the Slovak Republic (VEGA 2/0121/25), and the Slovak Academy of Sciences (CSIC-SAS-2023-02). The authors would like to acknowledge the contributions of all the researchers and laboratory staff who provided valuable insights and technical assistance throughout the study. Special thanks also go to the institutions and collaborators for their continuous support and for providing the necessary infrastructure and resources to carry out this work.

References

[1] R. E. Francis, G. Byrne, Duplex stainless steels – Alloys for the 21st century, Metals 11 (2021) 836. https://doi.org/10.3390/met11050836

[2] L. Pezzato, I. Calliari, Advances in duplex stainless steels, Materials 15 (2022) 7132. https://doi.org/10.3390/ma15207132

[3] L. O. Luengas, E. V. Morales, L. F. G. de Souza, I. S. Bott, Austenite transformation in duplex stainless steels under fast cooling rates, MS&T19 Proceedings (2019) 1010–1017. https://doi.org/10.7449/2019/mst_2019_1010_1017

[4] H. S. Abdo, A. H. Seikh, U. A. Samad, A. Fouly, J. A. Mohammed, Electrochemical corrosion behavior of laser welded 2205 duplex stainless steel in artificial seawater under different pH conditions, Crystals 11 (2021) 1025. https://doi.org/10.3390/cryst11091025

[5] T. R. Dandekar, A. Gupta, R. K. Khatirkar, R. Kumar, A. D. Gaikwad, Evolution of microstructure and texture in UNS S32750 super duplex stainless steel weldments, Transactions of the Indian Institute of Metals 74 (2021) 2267–2283. https://doi.org/10.1007/s12666-021-02274-x

[6] Á. Oñate, E. Torres, D. Olave, J. Ramírez, C. Medina, J. P. Sanhueza, M. Melendrez, V. Tuninetti, D. Rojas, Exploring the impact of cooling rate on microstructural features, mechanical properties, and corrosion resistance of a novel Nb-Stabilized super duplex stainless steel in shielded metal arc welding, Crystals 13 (2023) 1192. https://doi.org/10.3390/cryst13081192

[7] A. E. Odermatt, V. Ventzke, F. Dorn, R. Dinsé, P. Merhof, N. Kashaev, Effect of laser beam welding on microstructure, tensile strength and fatigue behaviour of duplex stainless steel 2205, Journal of Manufacturing Processes 72 (2021) 148–158. https://doi.org/10.1016/j.jmapro.2021.10.020

[8] S. F. Nabavi, A. Farshidianfar, H. A. Dalir, Comprehensive review on recent laser beam welding process: geometrical, metallurgical, and mechanical characteristic modeling, International Journal of Advanced Manufacturing Technology 129 (2023) 4781–4828. https://doi.org/10.1007/s00170-023-12536-1

[9] Y. Li, X. Zhou, S. Li, Residual stress and austenite recovery in super-duplex stainless steel after laser reheating, Materials Science and Engineering A (2021) 803. https://doi.org/10.1016/j.msea.2020.140575

[10] A. Baghdadchi, V. A. Hosseini, K. Hurtig, L. Karlsson, Promoting austenite formation in laser welding of duplex stainless steel—impact of shielding gas and laser reheating, Weld World 65 (2021) 499–511. https://doi.org/10.1007/s40194-020-01026-7

[11] C. Köse, C. Topal, Dissimilar laser beam welding of AISI 2507 super duplex stainless to AISI 317L austenitic stainless steel, Materials Science and Engineering: A 862 (2023) 144476. https://doi.org/10.1016/j.msea.2022.144476

[12] A. Ahola, J. Savolainen, L. Brask, T. Björk, Fatigue enhancement of welded thin-walled tubular joints made of lean duplex steel, Journal of Constructional Steel Research 218 (2024) 108738. https://doi.org/10.1016/j.jcsr.2024.108738

[13] L. Quackatz, I. Gornushkin, A. Griesche, T. Kannengiesser, K. Treutler, V. Wesling, In situ chemical analysis of duplex stainless steel weld by laser-induced breakdown spectroscopy, Spectrochimica Acta Part B: Atomic Spectroscopy 214 (2024) 106899. https://doi.org/10.1016/j.sab.2024.106899

[14] X. Li, A. M. A. Elsiddieg, A. M. Alqahtani, M. B. Ammar, A. Alzahrani, M. Hussien, S. Mahamad, Numerical and experimental evaluation of temperature field and melt flow in keyhole laser welding of dissimilar duplex stainless steel and nickel base alloy, International Journal of Thermal Sciences 214 (2025) 109858. https://doi.org/10.1016/j.ijthermalsci.2025.109858

[15] M. Keskitalo, K. Mäntyjärvi, J. Sundqvist, J. Powell, A. F. H. Kaplan, Laser welding of duplex stainless steel with nitrogen as shielding gas, Journal of Materials Processing Technology 216 (2015) 381–384. https://doi.org/10.1016/j.jmatprotec.2014.10.004

[16] L. Wang, T. Xu, Z. Zhu, L. Zhang, G. Mi, X. Ma, Effects of a new dual-beam oscillating laser welding technique for aluminum alloy joints: Microstructure, properties, and formation mechanism, Journal of Materials Processing Technology 340 (2025) 118883. https://doi.org/10.1016/j.jmatprotec.2025.118883

[17] J. Chao, Z. Hua, K. Sun, L. Wang, X. Ma, G. Mi, G. Zeng, Power ratio optimization in dual-beam laser welding of Ti-modified SiCp/2A14 composites: Impact on molten pool flow and microstructure, Journal of Materials Research and Technology 36 (2025) 7589–7602. https://doi.org/10.1016/j.jmrt.2025.05.006

[18] N. Li, Q. Lang, Y. Dong, C. Wang, T. Li, H. Wang, L. Liu, Evolution of bonding mechanism and fracture mechanism of Ti alloy-steel joint by dual-beam laser welding using Mg-RE (RE=Gd, Y) filler, Journal of Materials Research and Technology 28 (2024) 1137–1148. https://doi.org/10.1016/j.jmrt.2023.12.083

[19] A. Sajid, S. Joonghan, Improvement in weld quality of Al and Cu joints using dual-beam laser welding, Journal of Manufacturing Processes 119 (2024) 499–510. https://doi.org/10.1016/j.jmapro.2024.04.010

[20] J. Lee, J. Jang, J. Park, S. H. Lee, Numerical and experimental analysis on the effect of ring beam-driven flow in coaxial dual-beam laser welding of aluminum alloy, International Communications in Heat and Mass Transfer 157 (2024) 107800. https://doi.org/10.1016/j.icheatmasstransfer.2024.107800

[21] J. Chao, Z. Hua, K. Sun, L. Wang, X. Ma, G. Mi, G. Zeng, Power ratio optimization in dual-beam laser welding of Ti-modified SiCp/2A14 composites: Impact on molten pool flow and microstructure, Journal of Materials Research and Technology 36 (2025) 7589–7602. https://doi.org/10.1016/j.jmrt.2025.05.006

[22] Y. Chen, K. Wang, J. Huang, X. Li, Y. Rui, Study on the mechanism underlying effect of scanning paths on healing performances in dual-beam laser welding,

Optics & Laser Technology 182 Part A (2025) 112074. https://doi.org/10.1016/j.optlastec.2024.112074
[23] Z. Lei, H. Cao, X. Cui, Z. Wen, L. Li, Q. Zhang, Study on the suppression of solidification cracks in narrow gap laser welding of high-strength steel based on dual-beam gradient control weld solidification, Journal of Materials Processing Technology 329 (2024) 118440. https://doi.org/10.1016/j.jmatprotec.2024.118440
[24] J. Sun, K. Dilger, Influence of thermal conductivity on the predicted temperature fields in welding of steels, International Journal of Thermal Sciences 202 (2024) 109066. https://doi.org/10.1016/j.ijthermalsci.2024.109066
[25] T. Fuhrich, P. Berger, H. Hügel, Marangoni effect in laser deep penetration welding of steel, J. Laser Appl. 13 (2001) 178–186. https://doi.org/10.2351/1.1404412
[26] B. Fotovvati, S. Wayne, F. Lewis, G. E. Asadi, A review on melt-pool characteristics in laser welding of metals, Advances in Materials Science and Engineering 2018 (2018) 920718. https://doi.org/10.1155/2018/4920718
[27] S. M. A. Noori Rahim Abadi, Y. Mi, F. Sikström, A. Ancona, I. Choquet, Effect of shaped laser beam profiles on melt flow dynamics in conduction mode welding, International Journal of Thermal Sciences 166 (2021) 106957. https://doi.org/10.1016/j.ijthermalsci.2021.106957
[28] Y. Ai, J. Liu, C. Ye, S. Han, Analysis of the dynamic behaviors of molten pool and keyhole for the oscillating laser welding of dissimilar materials stake welded T-joints with a gap, International Journal of Heat and Mass Transfer 232 (2024) 125877. https://doi.org/10.1016/j.ijheatmasstransfer.2024.125877
[29] X. Meng, S. N. Putra, M. Bachmann, M. Rethmeier, A statistical assessment of the laser energy absorption and keyhole stability in high-power laser welding, Journal of Manufacturing Processes 141 (2025) 885–896. https://doi.org/10.1016/j.jmapro.2025.03.053
[30] N. Sommer, F. Stredak, M. Wiegand, S. Böhm, Grain growth and precipitation behaviour of AISI 430 ferritic stainless steel subjected to pulsed laser beam welding using free-form pulse shaping, Weld World 67 (2023) 51–62. https://doi.org/10.1007/s40194-022-01398-y
[31] Y. Zhang, D. Zou, X. Wang, Y. Li, Y. Jiang, W. Zhang, L. Tong, Influence of cooling rate on δ-ferrite/γ-austenite formation and precipitation behavior of 18Cr-Al-Si ferritic heat-resistant stainless steel, Journal of Materials Research and Technology 18 (2022) 1855–1864. https://doi.org/10.1016/j.jmrt.2022.03.060
[32] M. Pariona, A. Taques, L. Woiciechowski, The Marangoni effect on microstructure properties and morphology of laser-treated Al-Fe alloy with single track by FEM: Varying the laser beam velocity, International Journal of Heat and Mass Transfer 119 (2018) 10–19. https://doi.org/10.1016/j.ijheatmasstransfer.2017.11.097
[33] Z. S. Mao, J. Chen, Numerical simulation of the Marangoni effect on mass transfer to single slowly moving drops in the liquid-liquid system, Chemical Engineering Science 59 (2004) 1815–1828. https://doi.org/10.1016/j.ces.2004.01.035.
[34] M. L. Gatto, A. Santoni, E. Santecchia, S. Spigarelli, F. Fiori, P. Mengucci, M. Cabibbo, The potential of duplex stainless steel processed by laser powder bed fusion for biomedical applications: A review, Metals 13 (2023) 949. https://doi.org/10.3390/met13050949
[35] L. Chen, T. Lindou, W. Hua, L. Zhiyu, J. Yiming, Influence of cooling rate on microstructure evolution and pitting corrosion resistance in the simulated heat-affected zone of 2304 duplex stainless steels, Corrosion Science 58 (2012) 168–174. https://doi.org/10.1016/j.corsci.2012.01.018
[36] C. Köse, C. Topal, Texture, microstructure and mechanical properties of laser beam welded AISI 2507 super duplex stainless steel, Materials Chemistry and Physics 289 (2022) 126490. https://doi.org/10.1016/j.matchemphys.2022.126490
[37] H. S. Abdo, A. H. Seikh, Mechanical properties and microstructural characterization of laser welded S32520 duplex stainless steel, Materials 14 (2021) 5532. https://doi.org/10.3390/ma14195532
[38] M. Ali, M. Ishak, S. N. Aqida, S. H. Abdulhadi, The effect of fiber laser parameters on microhardness and microstructure of duplex stainless steel, MATEC Web of Conferences 90 (2017) 01024. https://doi.org/10.1051/matecconf/20179001024
[39] G. Sivakumar, S. Saravanan, K. Raghukandan, Investigation of microstructure and mechanical properties of Nd:YAG laser welded lean duplex stainless steel joints, Optik 131 (2017) 1–10. https://doi.org/10.1016/j.ijleo.2016.11.062